ACS APPLIED NANO MATERIALS

www.acsanm.org Article

Ferroelectricity and Piezoelectricity of $Na_{0.5}Bi_{0.5}TiO_3$ Nanotube Arrays: Implications for Functional Electronic Devices

Zhe Zhu,* Yating Xu, Junpeng Li, and Guozhong Cao*

Cite This: *ACS Appl. Nano Mater.* 2021, 4, 1294−1304 Read Online

ACCESS | Metrics & More | Article Recommendations | Supporting Information

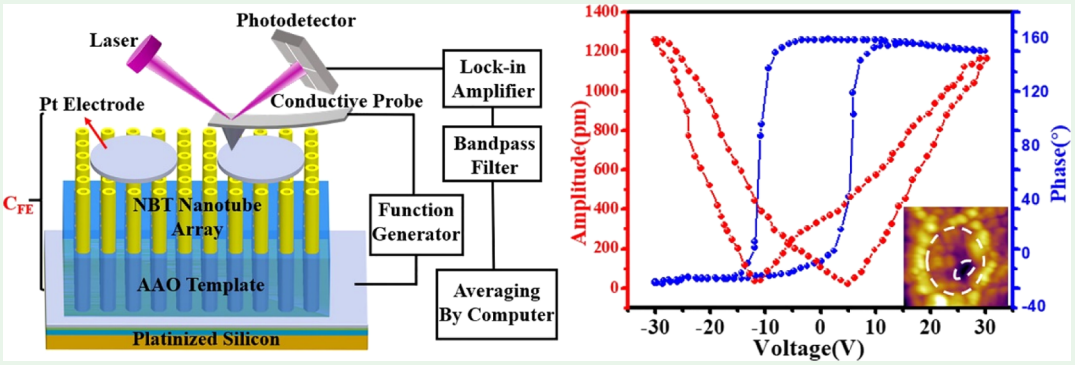

ABSTRACT: Piezoelectric and ferroelectric properties of lead-free sodium bismuth titanate $Na_{0.5}Bi_{0.5}TiO_3$ (NBT) nanotube arrays were studied using piezoresponse force microscopy. The nanotube arrays prepared by sol filling in the porous anodic aluminum oxide template with an exposure height of 30−55 nm and vertical arrangement demonstrated enhanced piezoelectric properties compared with the other nanotube structures and a large piezoelectric coefficient with regular domain states. We further prepared a metal/NBT nanotube arrays/metal capacitor for the study of ferroelectric and piezoelectric properties. The piezoelectric properties of NBT nanotube arrays were found to be much improved in a capacitor and finite element modeling attributes such improvement to the uniform electric potential distribution from the tip of the nanotube in the capacitor. The improved piezoelectric properties could make NBT nanotube arrays as a promising candidate for piezoelectric nanostructure devices.

KEYWORDS: *$Na_{0.5}Bi_{0.5}TiO_3$, nanotube arrays, ferroelectricity, piezoelectricity, piezoresponse force microscopy, finite element*

Because of the environmental protection and biocompatibility, lead-free ferroelectric materials[1−3] especially $Na_{0.5}Bi_{0.5}TiO_3$ (NBT)[4,5] are considered to be an excellent candidate for piezoelectric materials because of its strong piezoelectric properties with relatively large remanent polarization at room temperature.[6] On the other hand, with the rapid development of contemporary science and technology to the nanometer field and the trend of miniaturization of device sizes, researchers have conducted many experiments in ferroelectric materials such as thin films,[7] nanowires,[8] nanofibers,[9] and nanotubes.[10] One-dimensional (1D) nanostructured materials, especially nanotubes, are not only the smallest low-dimensional structure of electron transmission, but also suffer less from the clamping effect on the piezoelectric response, so they are expected to show higher information storage capabilities[10−13] to be used in the fields of microelectronics [ferroelectric random access memory (FeRAM)[14−17]] and micro-electro-mechanical systems (MEMS).[18,19] Compared with single or randomly arranged 1D nanostructured materials, vertically ordered ferroelectric nanotube arrays have greater potential applications, such as in one-transistor−one-capacitor (1T−1C) type FeRAM,[20−22] which is more advantageous in reducing crosstalk and uniformizing the electric field distribution. On the one hand, each nanotube of the array structure has a certain distance from each other so that each nanotube can store a bit of data, which greatly increases the information storage density of the device. On the other hand, because of its unique shape and surface effect, a strong depolarization field along the nanotube diameter will be generated on the inner and outer surface of the nanotube, forcing the polarization direction to be distributed only along the axial direction, which is conducive to improving the effective piezoelectric coefficient d_{33}, also the storage window of 1T−1C nonvolatile ferroelectric memory.

At present, the sol−gel template method is helpful for the preparation of one-dimensional nanotube arrays with different

Received: October 27, 2020
Accepted: January 14, 2021
Published: January 24, 2021

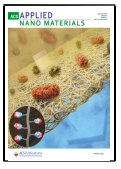

https://dx.doi.org/10.1021/acsanm.0c02878
ACS Appl. Nano Mater. 2021, 4, 1294−1304

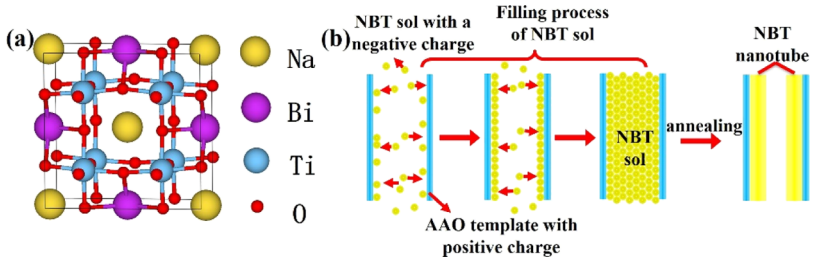

Figure 1. (a) NBT crystal structure (b) schematic illustration of the nanotube synthesis process.

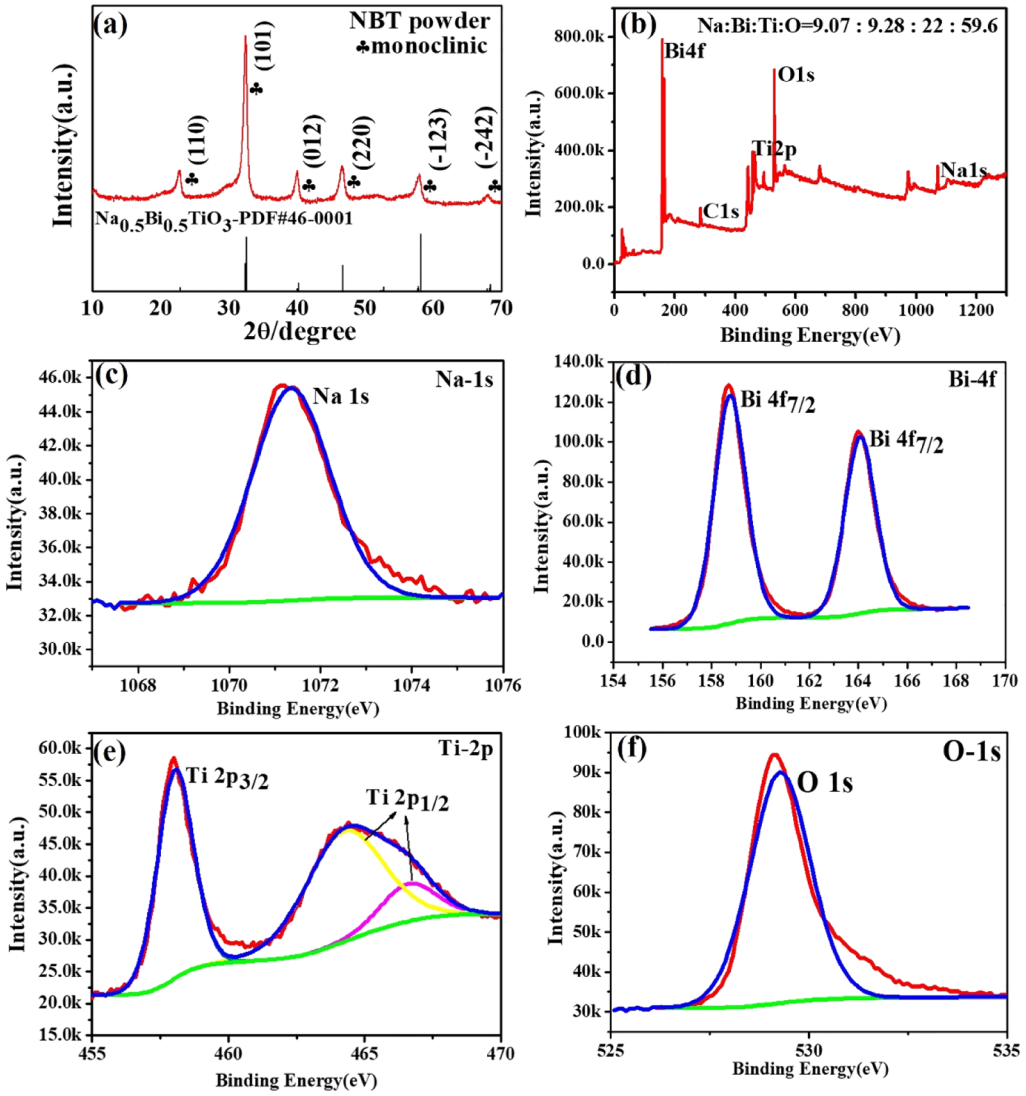

Figure 2. (a) XRD patterns of the NBT powder (PDF#46-0001). XPS of the NBT powder: (b) survey scan, (c) Na 1s, (d) Bi 4f, (e) Ti 2p, and (f) O 1s.

diameters, wall thicknesses, complex chemical components, and user-defined positions.[23] It usually includes a few phases as follows: precursor preparation, sol-filling process, and annealing and etching processes. Among them, the sol-filling process, which requires a high filling rate, directly determines the quality of nanotubes and is a key step in preparing ferroelectric nanotube arrays. Moreover, the selection of etching parameters during the etching process will generate different exposure heights of the nanotube, which affects the effective contact area between the nanotube array and top electrode in a capacitor structure.

Tang et al.[24] and Ianculescu et al.[25] prepared a $CoFe_2O_4$–$Pb(Zr_{0.52}Ti_{0.48})O_3$ composite coaxial nanotube array and a $BaTiO_3$ doped with 5 mol % Ce^{3+} nanotube array using the sol–gel template with the sol-filling process of immersion deposition and the nanotube arrays embedded in the template were obtained after the etching process. They only focus on the magnetoelectric coupling measurement and the characterization of the ferroelectric and piezoelectric properties of a single nanotube. Zhong et al.[26] prepared a $BiScO_3$–$PbTiO_3$ nanotube array using the sol–gel template and the nanotube arrays with aggregation states were obtained by etching with

https://dx.doi.org/10.1021/acsanm.0c02878
ACS Appl. Nano Mater. 2021, 4, 1294–1304

0.5 mol/L NaOH solution. The relationship between the tube wall thickness and piezoelectric property was specially studied. Zhou et al.[27] also prepared a $K_{0.5}Na_{0.5}NbO_3$ nanotube array using the sol−gel template with the sol-filling process of negative pressure deposition and obtained a nanotube array with aggregation states by etching with 4 mol/L NaOH solution. Kim et al.[28] prepared ultrathin-walled $Pb(Zr,Ti)O_3$ nanotube arrays by template sol filling with spin coating and investigated the relationship between the aspect ratio of nanotubes and the etching time of the NaOH solution. However, it is difficult to prepare a nanotube array with controlled wall thickness and a certain exposure height.

In recent years, there have been a large number of literature reports on the ferroelectric and piezoelectric properties of NBT ceramics,[29] thin films,[30] and nanofibers,[31] but there are few reports on the properties of NBT nanotube array structures. In this paper, we report on the fabrication of lead-free $Na_{0.5}Bi_{0.5}TiO_3$ (NBT) nanotube arrays using different sol-filling processes, and the structural, ferroelectric, and piezoelectric properties of the NBT nanotube arrays with different exposure heights have been systematically investigated using piezoresponse force microscopy (PFM). It is expected that the present research may offer useful guidelines to the design and application of ferroelectric and piezoelectric NBT and NBT-based nanostructure devices.

RESULTS AND DISCUSSION

The crystal structure diagram of NBT and the synthesis process of nanotube are shown in Figure 1. Figure 1a is the crystal structure diagram of NBT. It can be seen that NBT is A-bit complex perovskite-type relaxor ferroelectrics whose general formula is ABO_3. Ti is located in the body center, O is located in the face center, and Na and Bi occupy the apex of the cell. Figure 1b shows the schematic illustration of the nanotube synthesis process. The negatively charged NBT precursor is adsorbed in the holes of positively charged anodic aluminum oxide (AAO) template under the action of negative pressure and centrifugal force, and then formed into nanotubes after annealing crystallization.

After the NBT precursor was annealed at 700 °C, the crystallized NBT powders were obtained. Figure 2 shows the X-ray diffraction (XRD) and X-ray photoelectron spectroscopy (XPS) figures of the powders. The XRD patterns of NBT powders are obtained in a Bragg angle (2θ) range of 10−70°. All diffraction peaks in Figure 1a can be well indexed to (110), (101), (012), (220), (−123), and (−242), and the phase structure (according to JCPDS card no. 46-0001) is the monoclinic perovskite phase without detectable secondary phases, indicating that the powders have a typical perovskite structure and good crystallization. XPS measurement was performed to study the chemical state of the NBT powders. The XPS spectra of Bi 4f, Na 1s, Ti 2p, and O 1s of all the tested BNT powders are shown in Figure 2b−f The C 1s peak is at 284.38 eV and used as a reference standard in the XPS study. Figure 2b shows the survey scan of the NBT powders, it contains sodium, bismuth, and titanium oxygen and the atomic ratio is about 9.07:9.28:22:59.6, which is similar to the ratio of each element in NBT. Figure 2c shows that the binding energy of Na 1s in the NBT powders is 1171.35 eV. Figure 2d shows that the corresponding peaks for metallic Bi (0) and Bi (+3) in BNT are 158.75 and 164.07 eV, respectively.[32,33] The locations of the Ti $2p_{1/2}$ spectrum at 464.22 eV are attributed to the Ti^{4+} oxidation state, and the binding energies at 458.03 and 466.59 eV correspond to Ti^{3+} in Figure 2e.[34] Figure 2f presents the O 1s peaks of all the measured NBT powders and the peaks at 529.7 eV are attributed to oxygen in the perovskite lattice.[35] Therefore, the chemical formula for this powders can be written as $[Bi^{0+},Bi^{3+}]_{0.5}Na_{0.5}[Ti^{3+},Ti^{4+}]O_3$.[36]

Figure 3 shows the SEM images of NBT nanotube arrays after etching for 7 h with 5 wt % H_3PO_4 solution with different

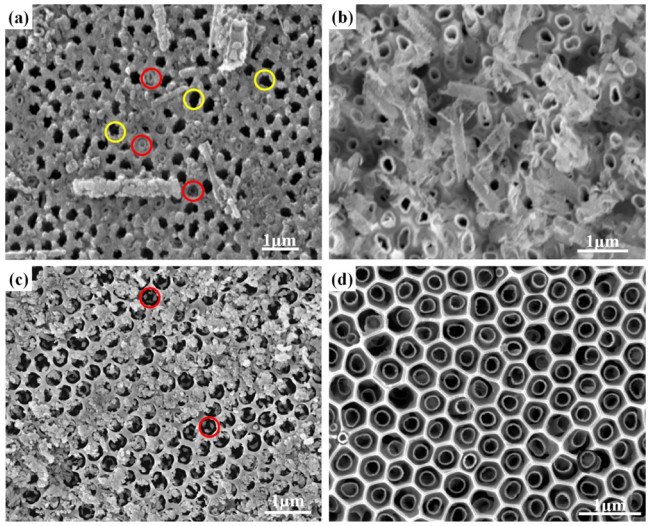

Figure 3. SEM images of NBT nanotube arrays prepared by different filling methods: (a) immersion deposition, (b) negative pressure deposition, (c) spin-coating deposition, and (d) improved method after etching by 5 wt % H_3PO_4 solution for 7 h.

sol-filling methods. In Figure 3a for the immersion deposition, there are only a few nanotubes (marked by red circle) within the AAO template and most of the area is hollow (marked by a yellow circle). When prepared using the immersion method, the driving force of the filling process is only the template's adsorption. The precursor first forms droplets as it enters the template hole, and the smaller the droplet radius is, the greater the additional pressure will be. Therefore, the capacity of adsorption of the template is difficult to overcome the additional pressure generated from the surface of the droplet and the original atmospheric pressure in the hole, so that the filling rate is very low.

Figure 3b shows the nanotube array structure prepared using the negative pressure method. It can be seen that the filling rate of the nanotube is greatly improved. This is because the atmospheric pressure in the hole and the surface tension of the precursor are overcome by the downward negative pressure, which generates a downward external force to the precursor leading a better sol filling rate compared with the immersion method. However, because of the lack of a force pointing to the inner wall of the hole, the formed nanotubes are disorderly distributed and have an irregular shape. In Figure 3c for the spin-coating method, the filling rate of the nanotube is similar to that of the negative pressure method, but the tube wall of the nanotube is discontinuous. During the spinning coating, it will make the atmospheric pressure in the template hole uneven and prevent the precursor from forming droplets. So that the template's adsorption force is easier to make the precursor fill into the area of low pressure and the atmospheric pressure and will discharge from the high pressure, leading to the increase of the filling rate. However, under the large centrifugal force, the tube wall of the formed nanotube is very

https://dx.doi.org/10.1021/acsanm.0c02878
ACS Appl. Nano Mater. 2021, 4, 1294−1304

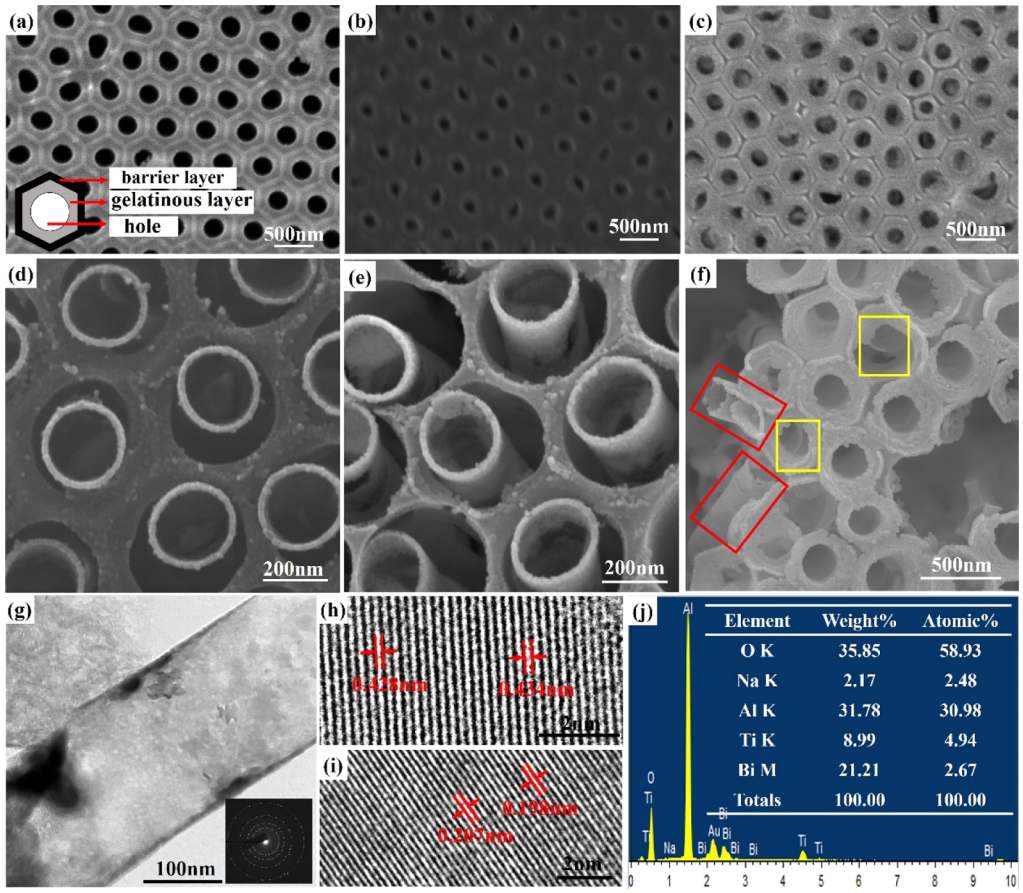

Figure 4. Structural characterization of NBT nanotube arrays prepared using the improved method. (a) SEM images of the blank AAO template. (b) NBT-gel filled with the template. (c) Composite structure of the NBT/AAO nanotube array after annealing. SEM images of the NBT/AAO nanotube etched by 1.8 mol/L NaOH at different times: (d) 40, (e) 43, and (f) 45 min. (g) TEM images of NBT nanotubes and the inset of the SAED pattern. HRTEM images of (h) (110) and (i) (220) crystal planes. (j) Energy-dispersive spectrum (EDS) showing the presence of elements in nanotube arrays.

thin, so that the final products will shrink and break after annealing, resulting in the existence of discontinuous nanotubes. For the improved method shown in Figure 3d, the nanotube has a high filling rate, a regular shape, and neat arrangement. The improved method is the combination of the negative pressure method and the spin-coating method. First, the negative pressure method is used to overcome the atmospheric pressure in the template hole and the surface tension of the precursor, and a downward external force is exerted on the precursor to make more precursor fill into the template. Then, the precursor is applied with a centrifugal force directed to the inner wall of the hole using a spinning coating device to form a regular shape of the nanotube, and the thickness of the nanotube wall can also be controlled accurately by the spinning rate.

The properties of reactants, the concentration of the etching solution, and the reaction time are the main factors affecting the etching degree of the AAO template and the exposure height of NBT nanotube arrays.[37,38] In order to find the suitable etching parameters, which can obtain the NBT nanotube array with an optimum exposure height, we used 5 wt % H_3PO_4 solution and different concentrations of the NaOH solution under different etching times to etch the NBT nanotubes embedded in the AAO template prepared with the improved sol-filling method (see S1−S4). Figure 4a is a SEM image of a blank AAO template. It can be seen that the diameter of the template hole is uniform. The template is composed of two layers, namely the gelatinous layer and the barrier layer[37] shown in the lower left corner of Figure 4a. In Figure 4b, the NBT gel is fully filled into each AAO template hole after drying. After the gel was annealed at a high temperature of 700 °C, the crystallized NBT nanotube array embedded in the AAO template had an obvious longitudinal shrinkage shown in Figure 4c because of the evaporation of volatile substances in the precursor solution. Figure 4d−f are FESEM images of the NBT/AAO nanotube arrays etched by 1.8 mol/L NaOH solution for 40, 43, and 45 min, respectively. In Figure 4d, it is clearly observed that the gelatinous layer of the AAO template was completely dissolved, and NBT nanotubes were flush with the template hole. The wall thickness and outer diameter of the nanotube are ∼25 and ∼250 nm, which are bigger than the template hole (200 ± 20 nm). The reason is that a weakly acidic NBT precursor with a certain corrosion effect on the gelatinous layer can enlarge the hole of the template. In Figure 4e, because of the prolonged etching time, the barrier layer of the AAO template was dissolved partially, which makes the nanotube array stick out of the template with a certain exposure height. When the etching time continued to be 45 min, the nanotubes in Figure 4f mainly show two distribution states. Some (marked by a red square) are disorderly state because the gelatinous layer and the barrier layer were completely dissolved. Others (marked by

https://dx.doi.org/10.1021/acsanm.0c02878
ACS Appl. Nano Mater. 2021, 4, 1294−1304

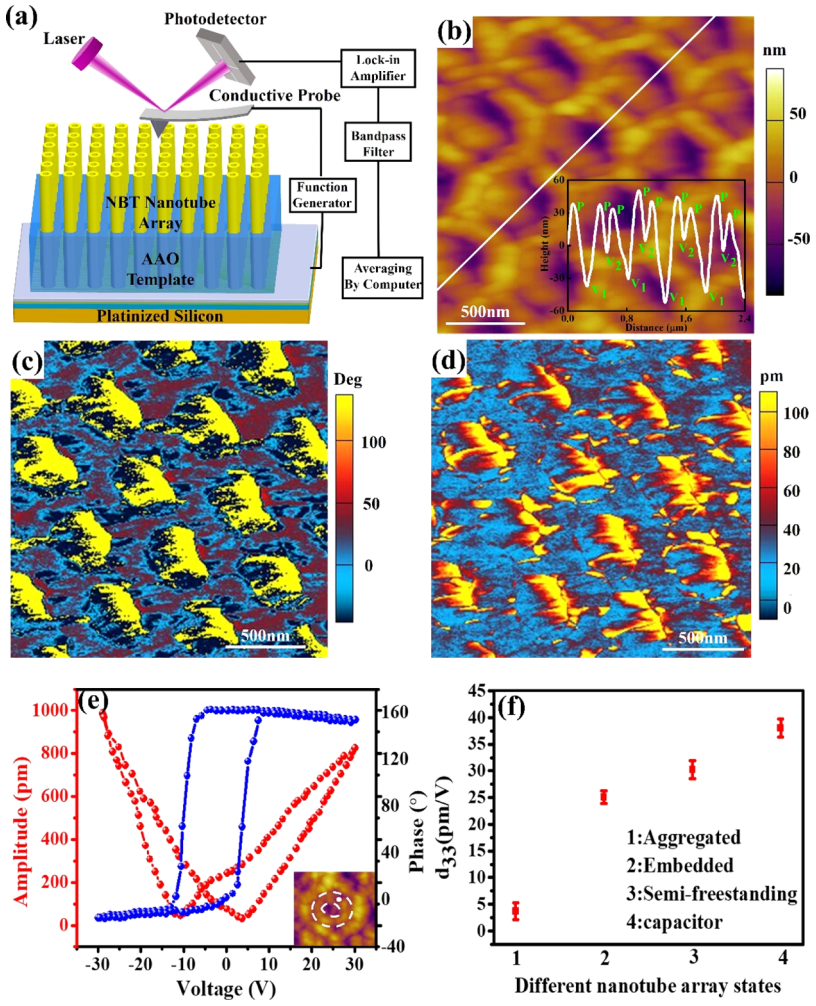

Figure 5. (a) Schematic drawing of the PFM measurement configuration. (b) Topography image of NBT nanotube arrays with an exposure height of 30−55 nm. (c) Phase image, (d) amplitude image, and (e) amplitude butterfly curve and phase hysteresis of NBT nanotube arrays with an exposure height of 30−55 nm. (f) Error bar diagram of the d_{33} value of the nanotube array structure in different states.

a yellow square) are still in the template with the different length and partially corroded with the template itself because of the total dissolution of the gelatinous layer and partial dissolution of the barrier layer. From the etching results, it can be seen that both H_3PO_4 and NaOH have the same corrosion effect on the gelatinous layer of the template, while NaOH has a better corrosion effect on the barrier layer than H_3PO_4 and the best corrosion parameter is etching for 43 min at 1.8 mol/L NaOH. In Figure 4g, the transmission electron microscopy (TEM) image shows the individual nanotube with a hollow morphology and a thin tube wall. However, the microstructure can be hardly visualized. The inset of Figure 4g shows a typical polycrystalline structure pattern of selected area electron diffraction (SAED). It is worth noting that the diffraction rings have brighter and discontinuous spots indicating good crystallinity. The TEM images of the completely corroded nanotube array structure prepared using different preparation methods are shown in Figure S5. From high-resolution TEM (HRTEM) images in Figure 4h,i, the lattice spacings of 0.428 and 0.434 nm correspond to the (110) crystal plane and the lattice spacings of 0.198 and 0.207 nm correspond to the (220) crystal plane of monoclinic NBT. The clear lattice fringes also indicate good crystallinity. The EDS in Figure 4j shows a detailed elemental composition of NBT nanotubes. The EDS shows the atomic ratio of each element, among which the proportion of the aluminum element is 30.98%. Therefore, it can be deduced that the proportion of the O element in the AAO template is 46.47%. Then, the element ratio of Na, Bi, Ti, and O in NBT nanotubes can be calculated and is approximately equal to 1:1:2:6, which is consistent with the atomic ratio of $Na_{0.5}Bi_{0.5}TiO_3$.

The original domain state and piezoelectric property of NBT nanotube arrays with a certain exposure height were measured and the results are shown in Figure 5a−e. For a comparison, the same measurement for the blank AAO template, the NBT nanotubes embedded in the template, and the NBT nanotube arrays with a disordered aggregation state are also shown, respectively (see S6−S8). Figure 5a is a schematic drawing of the PFM measurement configuration. The topography images, piezoelectric phase, and amplitude of NBT nanotube arrays with a certain exposure height are shown in Figure 5b−d. From the cross-sectional profile in Figure 5b, peak (P), valley (V_1), and valley (V_2) represent the tube wall position of the nanotube, the hole position of the nanotube, and the template position, respectively. The height difference from V_2 to P is the exposure height of the nanotube, that is, 30−55 nm. The distance between P on both sides of V_1 is the outer diameter of the nanotube ∼360 nm, which is larger than the SEM result.

https://dx.doi.org/10.1021/acsanm.0c02878
ACS Appl. Nano Mater. 2021, 4, 1294−1304

The reason is that the scan process between the tip and the nanotube as mentioned above leads to the difference. The inner diameter of the nanotube can be obtained to be ~200 nm by subtracting the half peak width (~80 nm) of the peaks on both sides of the V_1 from the distance between the peaks P, which is consistent with the inner diameter of the nanotube measured by SEM. The multicolor contrasts in Figure 5c (yellow and black) and Figure 5d (red and yellow) represent the polydomain structures within the nanotube and these regular regions also correspond to the topography of nanotube arrays with the exposure height shown in Figure 5b. Another notable phenomenon is that the domain states of the outer and inner nanotube wall in Figure 5c,d can not be distinguished clearly. It may relate to the way the probe contacts with the nanotube array during the scanning process. At the beginning, the tip touched the outer wall of the nanotube, and the nanotube bends under the tip force, increasing the contact area between the tip and the nanotube, thus increasing the piezoelectric response. When the tip continued to scan, the nanotube returned to its original upright state accompanied by the decreasing contact areas between the tip and the nanotube and decreasing the piezoelectric response.[39,40]

The PFM amplitude−voltage butterfly curve (red) and phase−voltage hysteresis loop (blue) are given in Figure 5e and the PFM tip was located at the outer wall position of a single NBT nanotube during the measurement marked by the white dot shown in the inset of Figure 5e. The butterfly-shape curve appears symmetrical indicating the certain piezoelectric properties.[41] It can be calculated that the maximum effective piezoelectric coefficient d_{33} is about 30.7 pm/V. On the other hand, the phase hysteresis loop presents about 180° domain switching at ± 30 V. Figure 5f shows the error bar diagram of the d_{33} value of nanotube array structure in different states.

For further comparison, Table 1 gives the effective piezoelectric coefficients of NBT materials with different geometric shapes. d_{33} in Figure 4e is higher than those in Figures S7 and S8 because of the good contact between the arranged nanotubes and the conductive probe. It is also better than the other 1D ferroelectric materials reported in the literature, such as the NBT nanofiber (d_{33} = 15 pm/V)[31] and the NBT nanowire (d_{33} = 24 pm/V).[42] One-dimensional nanomaterials reported in the literature are flat on the substrate with a large clamping effect of the substrate, and thus the depolarization field causes the domain structure to distribute along the axial direction (i.e., the in-plane direction). When the external electric field is applied along the radius direction, the direction of the external electric field is perpendicular to the direction of the polarization vector, which is not conducive to the polarization inversion. Moreover, the direction of the external electric field is parallel to the direction of the depolarization field, and the depolarization field will weaken the effect of the external electric field, resulting in a large coercive field or even imprint. However, because of the empty structure and vertical arrangement, the nanotube array is subject to a small clamping effect. In this case, the depolarization field will be along the in-plane direction. Therefore, the domain structure of the nanotube array is less affected by the depolarization field, and easier to be switched at the same electric field. Although the piezoelectric coefficient of the NBT nanotube array structure with a certain exposure height is much lower than that of the ceramics and 30% smaller than that of the thin films, it still has some advantages as ferroelectric random memory because of independent distribution and vertical arrangement.

Table 1. Comparison of Piezoelectric Coefficients of NBT Materials with Different Geometric Morphologies

materials	state	d_{33} (pm/V)	refs
nanotube arrays	embedded (Figure S6)	24.8	this work
	semifreestanding (Figure 3)	30.7	this work
	aggregated (Figure S7)	3.4	this work
	capacitor (Figure 6)	38.5	this work
ceramics	none	79	29
films	none	56	30
nanofibers	none	15	31
nanowires	none	24	42

Based on the NBT nanotube array with an optimum exposure height, we prepared a metal/NBT nanotube array/metal capacitor structure and determined the P−E loops and piezoelectric coefficients to further check the ferroelectricity of nanotube arrays. As a schematic drawing of the ferroelectric testing configuration shown in Figure 6a, we first covered a metal mask on the template of the NBT/AAO composite structure, and deposited a Pt top electrode with a thickness of about 100 nm and a diameter of 200 μm, and then detected the ferroelectricity using a ferroelectric analyzer. The inset on the left of Figure 6a is the photo of ferroelectric capacitor during the testing and the right is an optical microscope image of the Pt top electrode with a uniform size deposited on the NBT nanotube array. Figure 6b is the P−E curve of the ferroelectric capacitor under different electric fields. It is found that the coercive field (E_c) and the remanent polarization (P_r) are significantly enhanced with the increase of the driving voltage. The NBT nanotube capacitor exhibits well-saturated hysteresis loops with P_r and E_c values of about 1.36 μC/cm^2 and 6.74 kV/cm under a maximum applied electric field of 20 kV/cm. Considering the geometrical dependence of P_r, the effective contact area between the Pt electrode and the NBT nanotubes was calculated to be about 9.7% of the total Pt electrodes. Therefore, the normalized P_r was estimated to be 14.9 μC/cm^2. For further comparison, Table 2 summarizes the ferroelectric performance parameters of some ferroelectric capacitors based on the perovskite thin films and one-dimensional materials. We found that the normalized P_r of the NBT nanotube array is comparable to that of the NBT thin film prepared using the sol−gel method.[7,43] Compared with other lead-free perovskite nanotube array capacitors,[44−46] our results also show a better P_r value of 14.9 μC/cm^2 and is closer to the value of 17 μC/cm^2 for PZT nanotube arrays.[28] Nevertheless, the hysteresis loop is unsaturated. It may be because of a defect inside the NBT nanotube array during the preparation, such as oxygen vacancies,[47] which will bring a large leakage current and make the hysteresis loop not close. Besides that, the loop deviates along the x-axis to varying degrees. It could be because of the different shapes of the top and bottom electrodes (the top electrode is a concentric cylinder, and the bottom electrode is a Pt film) of the NBT nanotube array and the interface between the different Pt electrodes and the nanotube formed a nonferroelectric dead layer,[48] which concentrates the charge injected from the electrode to construct built-in electric field causing nonclosure and deviation of the hysteresis loop.

Figure 7 shows the piezoelectric properties of NBT nanotube arrays in the capacitor structure. Figure 7a is a

https://dx.doi.org/10.1021/acsanm.0c02878
ACS Appl. Nano Mater. 2021, 4, 1294−1304

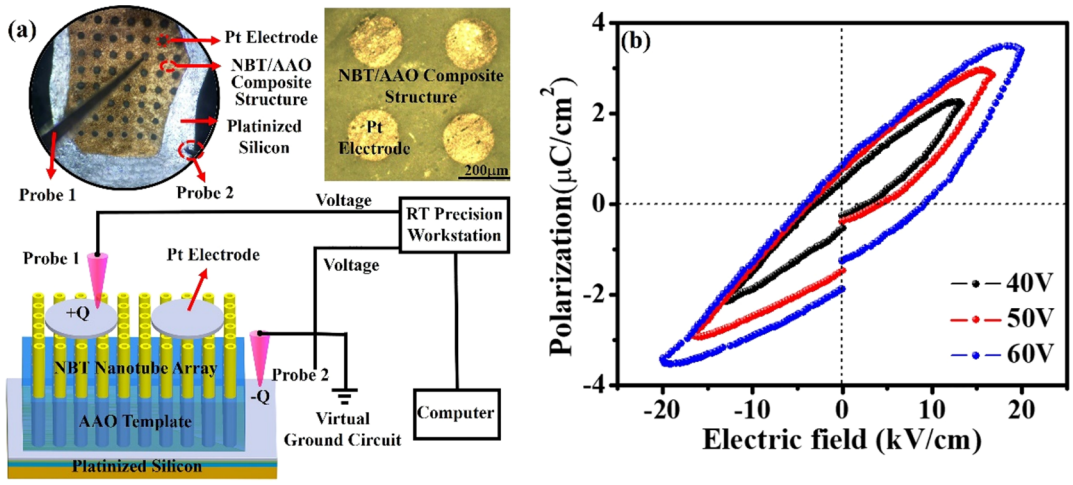

Figure 6. (a) Schematic of ferroelectric analyzer measurement on the nanotube capacitor. (b) *P*–*E* hysteresis loops of the nanotube array in the capacitor structure.

Table 2. Comparison of E_c and P_r (Nanotube Array Was Normalized) of Some Ferroelectric Capacitors Based on the Perovskite Materials

dimension	materials	structure	E_c (kV/cm)	P_r (μC/cm^2)	E (kV/cm)	refs
thin film	$Na_{0.5}Bi_{0.5}TiO_3$	Pt/NBT/Pt	94	12.6	none	7
	$Na_{0.5}Bi_{0.5}TiO_3$	LSCO/NBT/LSCO	47	15.6	250	43
nanotube arrays	$Pb(Zr,Ti)O_3$	(Ti/Au)/PZT/(Ti/Au)	86	17	400	28
	$Na_{0.5}Bi_{0.5}TiO_3$	Pt/NBT/Pt	6.7	14.9	20	this work
	$Bi_{3.15}Nd_{0.85}Ti_3O_{12}$	Pt/BNT/Pt	0.91	1.47	none	42
	$CoFe_2O_4$–$Bi_{3.15}Nd_{0.85}Ti_3O_{12}$	Pt/CFO-BNT/Pt	5	10	none	45
	$Bi_{3.15}Nd_{0.85}Ti_3O_{12}$	Pt/BNT/Pt	27	10	100	46
	$K_{0.5}Na_{0.5}NbO_3$	Au/KNN/Au	3.4	18.85	12.5	2

schematic drawing of the PFM measurement configuration. Compared with the phase images of the nanotube array without the top electrode (see Figure 5c), the domain structure of nanotube array with the Pt top electrode is easier to identify and shows a single domain structure in Figure 7b. The domain states of the NBT nanotube array in the capacitor structure are mainly dark red, which represents a-domains of the polarization vector along the horizontal direction. The domain boundary marked by the white circle is also continuous, representing the nanotube array with exposure height is more regularly distributed in the capacitor structure.[49] In Figure 7c, the NBT nanotube array in the capacitor structure has a stronger piezoelectric response compared with that shown in Figure 5d. From topography image in Figure 7d, there are a lot of Pt metal particles on the surface of the NBT nanotube array after deposition, while the hollow part of the nanotube inner wall is obviously reduced by filling with some metal particles. For piezoelectricity measurement, we selected different single nanotubes to test at different points of the Pt top electrode marked by the white dotted line in the inset of Figure 7e and the amplitude–voltage butterfly curve (red) and phase–voltage hysteresis loop diagram (blue) of the NBT nanotube array in capacitor structure are shown in Figure 6e. There are more complete 180° domain switching in the phase hysteresis loop and more symmetrical butterfly curve, indicating the better ferroelectricity and piezoelectric performance for the nanotube array in the capacitor structure. The effective piezoelectric coefficient d_{33} is about 38.5 pm/V. It is found that the effective piezoelectric coefficient of the NBT nanotube array in the capacitor structure is improved by approximately 26% compared with the other pure NBT nanotube arrays.

In order to further explain the different mechanisms of piezoelectric properties for NBT nanotube arrays and NBT nanotube arrays in the capacitor structure, the finite element models (FEM) of single NBT nanotubes with a bottom electrode and single NBT nanotubes with the top and bottom electrodes were established to calculate the electric potential distributions. The Maxwell equations are solved using the Numerical simulation method and the results are shown in Figure 8. Figure 8a is the model of single NBT nanotubes with a bottom electrode and Figure 8b is the electric potential distribution in three dimensional and cross-sectional views. It can be seen that the electric potential within nanotubes has a ununiform distribution only in the local tip contact area when an electric field is applied, and in most other areas the potential is 0. Figure 8c,d shows a FEM model of the single NBT nanotube with the top and bottom electrodes, and the potential distribution from the three dimensional and cross section views. The potential distribution is uniform in both the tip contact region and the noncontact region and decreased uniformly along the longitudinal length of the nanotube. Based on the simulation results, the experimental phenomenon can be explained that only feedback signals from the surface layer of the pure nanotube array can be detected during PFM measurement, while for the capacitor structure, signals from the whole length direction of the nanotube can be detected. Therefore, the experimental results showed that the piezoelectric performance of NBT nanotubes in the capacitor structure was improved greatly.

https://dx.doi.org/10.1021/acsanm.0c02878
ACS Appl. Nano Mater. 2021, 4, 1294–1304

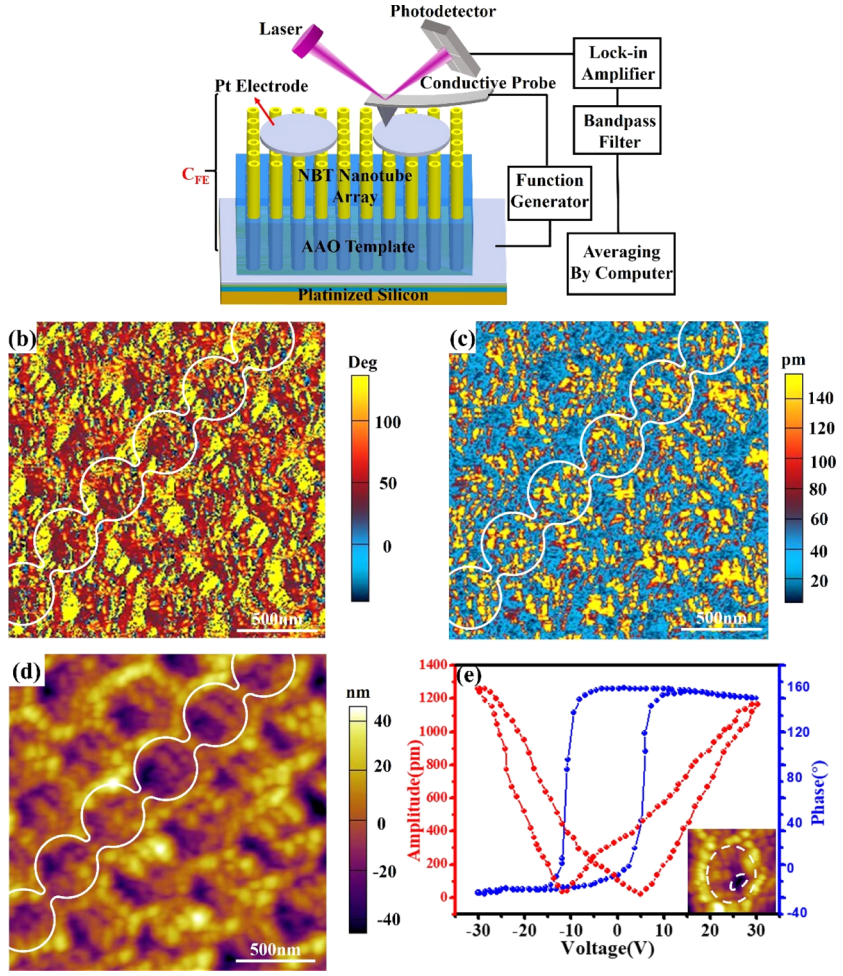

Figure 7. (a) Schematic drawing of the PFM measurement configuration. (b) Phase, (c) amplitude, and (d) topography images of nanotube capacitor. (e) Amplitude butterfly and phase hysteresis loops versus voltage of the nanotube array in the capacitor structure.

CONCLUSIONS

Compared with the nanotube arrays embedded in the template and with aggregation state, a nanotube array with an exposure height of 30−55 nm shows clear original domains and enhanced piezoelectric properties with a d_{33} value of 30.7 pm/V. NBT nanotube arrays in capacitor structures have a P_r value of 14.9 $\mu C/cm^2$, close to that of the PZT nanotube arrays, and a d_{33} value of 38.5 pm/V with a 26% improvement in piezoelectric performance compared with the pure nanotube array. FEM simulations explain that the more uniform distribution of potential within the NBT nanotube capacitor structure under the tip will exhibit a better piezoelectric performance than the NBT nanotube without a top electrode. It indicates 1D piezoelectric nanofibers may be a promising candidate for the realization of nanoscale lead-free piezoelectric devices for MEMS applications.

EXPERIMENTAL SECTION

Preparation of NBT Precursors. In this study, we selected bismuth nitrate pentahydrate ($Bi(NO_3)_3{\cdot}5H_2O$), tetrabutyl titanate ($Ti(OC_4H_9)_4$), ethylene glycol monomethyl ($CH_3OCH_2CH_2OH$), sodium acetate (CH_3COONa), acetic acid (CH_3COOH), and acetylacetone ($CH_3COCH_2COCH_3$) as preferred raw materials, and the detailed preparation process is as follows: first, 1.078 g $Bi(NO_3)_3{\cdot}5H_2O$ and 0.166 g CH_3COONa were dissolved in 15 mL $CH_3OCH_2CH_2OH$ and 3 mL CH_3COOH, respectively. Second, the CH_3COONa solution was added into the $Bi(NO_3)_3{\cdot}5H_2O$ solution, which was subsequently stirred for 20 min. After that, 1.375 g $Ti(OC_4H_9)_4$ and 1 mL $CH_3COCH_2COCH_3$ were added successively and stirred for 2 h at room temperature to form a uniform NBT precursor solution.

Preparation of NBT Nanotube Array by the Template Method. In order to obtain better NBT nanotube arrays, four different sol-filling methods including immersion deposition, negative pressure deposition, spin-coating deposition, and the improved method were used to prepare NBT nanotube arrays for comparison. The preparation processes of these four methods are described below.

Immersion Deposition. Firstly, a commercial AAO template (Shenzhen Topmembranes, pore diameter ~200 nm, thickness ~30 μm) was immersed in the NBT precursor solution for 5 days in order to make the NBT sol to fill into the template holes. Then, we took out the AAO template, wiped its surface with propanol, and dried it in an oven at 120 °C for 3 min. Finally, the products obtained in the previous step are placed in the muffle furnace for annealing treatment. The annealing process parameters are as follows: gradually heated from room temperature to 175 °C for 10 min, 400 °C for 10 min, and 700 °C for 1 h with a heating rate of 5 °C/min, and then cooled down to room temperature. The annealed product was etched with 5 wt % phosphoric acid (H_3PO_4) for 7 h to obtain the NBT nanotube array. The schematic drawing of the preparation process is shown in Figure S9a.

Negative Pressure Deposition. The AAO template was first immersed in the NBT precursor solution for 15 min, and then the NBT sol was sucked into the holes of the AAO template using the filter holder and a vacuum pump under a lower atmosphere pressure. The above steps were repeated 3−5 times, and the other steps were

https://dx.doi.org/10.1021/acsanm.0c02878
ACS Appl. Nano Mater. 2021, 4, 1294−1304

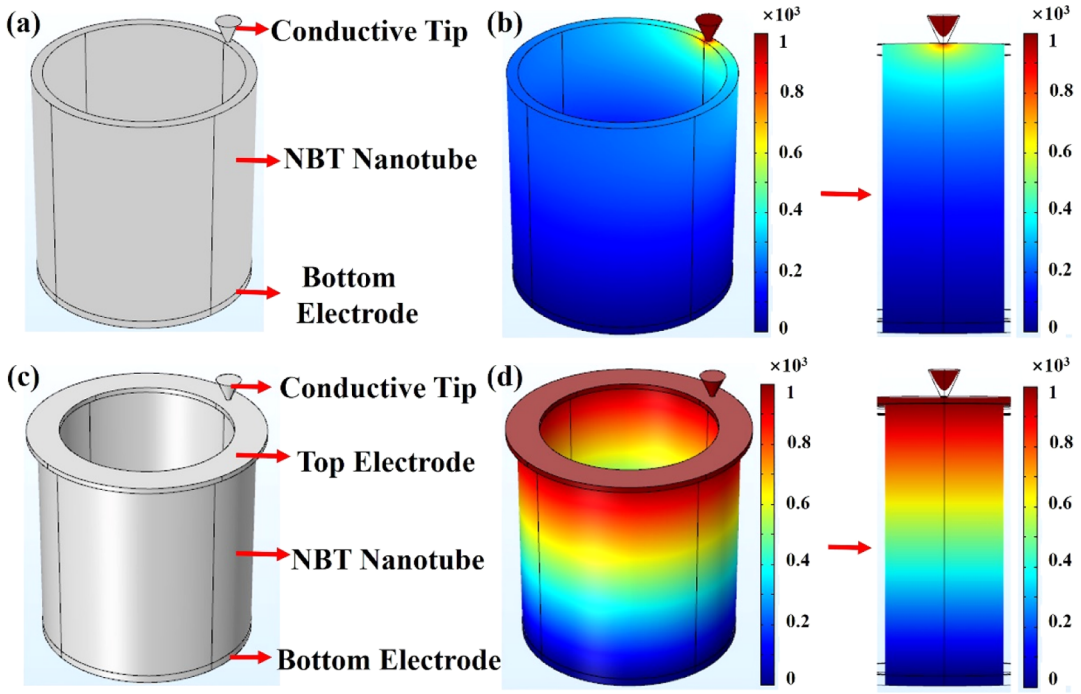

Figure 8. Potential distributions of NBT nanotubes and NBT nanotubes with the top electrode under the PFM tip. (a) Model of the NBT nanotube. (b) Potential distribution diagrams of the NBT nanotubes for the PFM tip contacting on the nanotube upper surface. (c) NBT nanotube with top electrode. (d) Potential distribution diagrams of NBT nanotubes with the top electrode for the PFM tip contacting on the electrode upper surface.

the same as the immersion deposition. The schematic drawing of the preparation process is shown in Figure S9b.

Spin-Coating Deposition. First, the AAO template was fixed on the upper surface of the Si substrate with polyimide tape and then the Si substrate was placed on the spin-coating table. Then, a small amount of NBT sol was dripped onto the AAO template to stand for 20 min and spinned at 500 rpm for 20 s and 3000 rpm for 60 s, which is repeated three to five times. The other steps were the same as the immersion deposition. The schematic drawing of the preparation process is shown in Figure S9c.

Improved Method. The AAO template was first immersed in the NBT precursor solution for 10 min and then the NBT sol was filled into the template holes under a negative pressure of $<10^{-1}$ MPa. Then, the Si substrate of which the AAO template was fixed on the surface was placed on the spin-coating table to spin at 500 rpm for 10 s and 3000 rpm for 60 s. Finally, the AAO template was took out to wipe its surface with propanol, and dry it in an oven at 120 °C for 3 min. The above steps were repeated three to five times, and the other steps were the same as the immersion deposition. The schematic drawing of the preparation process is shown in Figure S9d.

Materials Characterization. The phase structure of the NBT powder was characterized by XRD (D/MAX 2500, Rigaku, Japan). The exact stoichiometry and oxidation states of different constituents in the NBT powder were characterized by XPS (Thermo Kalpha; Thermo ESCALAB 250XI; Axis Ultra DLD Kratos AXIS SUPRA; PHI-5000versaprobeIII). The size and morphology of the products were observed using a scanning electron microscope (JSM-6610LV, JEOL, Japan) and a field-emission scanning electron microscope (MIRA3 LMU, Tescan, Czech). Crystallite size, shape, and lattice structure of a single NBT nanotube were observed by using a transmission electron microscope (JEM-2100, JEOL, Japan). The chemical composition of the specimens was confirmed using an energy-dispersive spectrometer. The original domain states and piezoelectric properties of the NBT nanotube arrays with different exposure heights were investigated using the PFM (MFP-3D Infinity, Asylum Research, USA) with a Ti/Ir-coated silicon cantilever (ASYELEC-01-R2, force constant 2.8 N/m, resonance frequency 75 kHz). Meanwhile, the *P*–*E* hysteresis loops and piezoelectric properties of NBT nanotube arrays with an optimum exposure height in the capacitor structure were measured by using a ferroelectric analyzer (RT6000S, Radiant Technologies, USA) and a piezoresponse force microscope.

■ ASSOCIATED CONTENT

Supporting Information

The Supporting Information is available free of charge at https://pubs.acs.org/doi/10.1021/acsanm.0c02878.

Microstructure of NBT nanotube arrays under different etching parameters, TEM images of NBT nanotubes under different preparation methods, the original domain state of the annealed blank AAO template, effects of different exposure heights on the original domain states and electrical properties of NBT nanotube arrays, and schematic diagrams of different sol-filling methods (PDF)

■ AUTHOR INFORMATION

Corresponding Authors

Zhe Zhu − *School of Materials Science and Engineering, Xiangtan University, Xiangtan, Hunan 411105, P. R. China;* orcid.org/0000-0002-0491-4665; Email: akzhuzhe@126.com

Guozhong Cao − *Department of Materials Science and Engineering, University of Washington, Seattle, Washington 98195, United States;* Email: gzcao@uw.edu

Authors

Yating Xu − *School of Materials Science and Engineering, Xiangtan University, Xiangtan, Hunan 411105, P. R. China*

Junpeng Li − *School of Materials Science and Engineering, Xiangtan University, Xiangtan, Hunan 411105, P. R. China*

https://dx.doi.org/10.1021/acsanm.0c02878
ACS Appl. Nano Mater. 2021, 4, 1294−1304

Complete contact information is available at:
https://pubs.acs.org/10.1021/acsanm.0c02878

Author Contributions

Z.Z. conceived the idea. Z.Z., Y.X., and J.L. synthesized the materials and performed materials characterization and PFM measurements. Y.X. performed the finite element theory analysis. Z.Z., Y.X., and G.C. wrote and revised the article with critical inputs from all other authors. All authors edited and approved the manuscript.

Notes

The authors declare no competing financial interest.

■ ACKNOWLEDGMENTS

This work was supported by the Scientific Research Foundation of Hunan Provincial Education Department [18B061].

■ REFERENCES

(1) Wu, J. Perovskite lead-free piezoelectric ceramics. *J. Appl. Phys.* **2020**, *127*, 190901.
(2) Qiao, L.; Li, G.; Tao, H.; Wu, J.; Xu, Z.; Li, F. Full characterization for material constants of a promising KNN-based lead-free piezoelectric ceramic. *Ceram. Int.* **2019**, *46*, 5641.
(3) Im, M.; Lee, W.-H.; Kweon, S.-H.; Nahm, S. New lead-free piezoelectric thin film fabricated using metal-oxide nanosheets at low temperature. *Ceram. Int.* **2019**, *45*, 21773−21780.
(4) Zheng, T.; Wu, J.; Xiao, D.; Zhu, J. Recent development in lead-free perovskite piezoelectric bulk materials. *Prog. Mater. Sci.* **2018**, *98*, 552.
(5) Wu, J. *Advances in Lead-Free Piezoelectric Materials*; Springer Nature Singapore Pte Ltd, 2018.
(6) Zhang, H.; Jiang, S.; Zeng, Y. Piezoelectric property in morphotropic phase boundary $Bi_{0.5}(Na_{0.82}K_{0.18})_{0.5}TiO_3$ leadfree thick film deposited by screen printing. *Appl. Phys. Lett.* **2008**, *92*, 152901.
(7) Bousquet, M.; Duclère, J.-R.; Champeaux, C.; Boulle, A.; Marchet, P.; Catherinot, A.; Wu, A.; Vilarinho, P. M.; Députier, S.; Guilloux-Viry, M.; Crunteanu, A.; Gautier, B.; Albertini, D.; Bachelet, C. Macroscopic and nanoscale electrical properties of pulsed laser deposited (100) epitaxial lead-free $Na_{0.5}Bi_{0.5}TiO_3$ thin films. *J. Appl. Phys.* **2010**, *107*, 034102.
(8) Zhou, X.; Jiang, C.; Chen, C.; Luo, H.; Zhou, K.; Zhang, D. Morphology control and piezoelectric response of $Na_{0.5}Bi_{0.5}TiO_3$ synthesized via a hydrothermal method. *CrystEngComm* **2016**, *18*, 1302−1310.
(9) Liu, B.; Lu, B.; Chen, X.; Wu, X.; Shi, S.; Xu, L.; Liu, Y.; Wang, F.; Zhao, X.; Shi, W. A high-performance flexible piezoelectric energy harvester based on lead-free $(Na_{0.5}Bi_{0.5})TiO_3$−$BaTiO_3$ piezoelectric nanofibers. *J. Mater. Chem. A* **2017**, *5*, 23634−23640.
(10) Ai, Z.; Lu, G.; Lee, S. Efficient photocatalytic removal of nitric oxide with hydrothermal synthesized $Na_{0.5}Bi_{0.5}TiO_3$ nanotubes. *J. Alloys Compd.* **2014**, *613*, 260−266.
(11) Zhou, Z.; Tang, H.; Sodano, H. A. Vertically aligned arrays of $BaTiO_3$ nanowires. *ACS Appl. Mater. Interfaces* **2013**, *5*, 11894−11899.
(12) Naumov, I. I.; Bellaiche, L.; Fu, H. Unusual phase transitions in ferroelectric nanodisks and nanorods. *Nature* **2004**, *432*, 737.
(13) Levi, B. G. Do atomic force microscope arrays have the write stuff? *Phys. Today* **2002**, *55*, 14−17.
(14) Auciello, O.; Scott, J. F.; Ramesh, R. The physics of ferroelectric memories. *Phys. Today* **1998**, *51*, 22−27.
(15) Cheong, S.-W.; Mostovoy, M. Multiferroics a magnetic twist for ferroelectricity. *Nat. Mater.* **2007**, *6*, 13.
(16) Cho, Y. Nanoscale ferroelectric information storage based on scanning nonlinear dielectric microscopy. *J. Nanosci. Nanotechnol.* **2007**, *7*, 105−116.
(17) Evans, P. R.; Zhu, X.; Baxter, P.; McMillen, M.; McPhillips, J.; Morrison, F. D.; Scott, J. F.; Pollard, R. J.; Bowman, R. M.; Gregg, J. M. Toward self-assembled ferroelectric random access memories: Hard-wired switching capacitor arrays with almost Tb/in.2 densities. *Nano Lett.* **2007**, *7*, 1134−1137.
(18) Lin, Y.; Liu, Q.; Tang, T.; Yao, X.; Huang, W. Wet chemical etching of lead zirconate titanate thin film for microelectro-mechanical systems applications. *Ferroelectrics* **2001**, *263*, 33.
(19) Masuda, K.; Lich, L. V.; Shimada, T.; Kitamura, T. Periodically-arrayed ferroelectric nanostructures induced by dislocation structures in strontium titanate. *Phys. Chem. Chem. Phys.* **2019**, *21*, 22756−22762.
(20) Zhang, X. Y.; Zhao, X.; Lai, C. W.; Wang, J.; Tang, X. G.; Dai, J. Y. Synthesis and piezoresponse of highly ordered $Pb(Zr_{0.53}Ti_{0.47})O_3$ nanowire arrays. *Appl. Phys. Lett.* **2004**, *85*, 4190−4192.
(21) Varghese, J.; Barth, S.; Keeney, L.; Whatmore, R. W.; Holmes, J. D. Nanoscale ferroelectric and piezoelectric properties of Sb_2S_3 nanowire arrays. *Nano Lett.* **2012**, *12*, 868−872.
(22) Luo, Y.; Szafraniak, I.; Nagarajan, V.; Wehrspohn, R. B.; Steinhart, M.; Wendorff, J. H.; Zakharov, N. D.; Ramesh, R.; Alexe, M. Ferroelectric lead zirconate titanate and barium titanate nanoshell tubes. *MRS Online Proceedings Library Archive*, 2003; p 782.
(23) Bernal, A.; Tselev, A.; Kalinin, S.; Bassiri-Gharb, N. Free-Standing Ferroelectric Nanotubes Processed via Soft-Template Infiltration. *Adv. Mater.* **2012**, *24*, 1160−1165.
(24) Tang, D.; Zeng, Z.; Zhou, Q.; Su, S.; Hu, D.; Li, P.; Lin, X.; Gao, X.; Lu, X.; Wang, X.; Jin, M.; Zhou, G.; Zhang, Z.; Liu, J. Ordered multiferroic $CoFe_2O_4$−$Pb(Zr_{0.52}Ti_{0.48})O_3$ coaxial nanotube arrays with enhanced magnetoelectric coupling. *RSC Adv.* **2017**, *7*, 29096−29102.
(25) Ianculescu, A.-C.; Vasilescu, C.-A.; Trupina, L.; Vasile, B. S.; Trusca, R.; Cernea, M.; Pintilie, L.; Nicoară, A. Characteristics of Ce^{3+}-doped barium titanate nanoshell tubes prepared by template-mediated colloidal chemistry. *J. Eur. Ceram. Soc.* **2016**, *36*, 1633−1642.
(26) Zhong, C.; Lu, Z.; Wang, X.; Li, L. Template-based synthesis and piezoelectric properties of $BiScO_3$-$PbTiO_3$ nanotube arrays. *J. Alloys Compd.* **2016**, *655*, 28−31.
(27) Zhou, D.; Gu, H.; Hu, Y.; Tian, H.; Wang, Z.; Qian, Z.; Wang, Y. Synthesis, characterization and ferroelectric properties of lead-free $K_{0.5}Na_{0.5}NbO_3$ nanotube arrays. *J. Appl. Phys.* **2011**, *109*, 114104.
(28) Kim, J.; Yang, S. A.; Choi, Y. C.; Han, J. K.; Jeong, K. O.; Yun, Y. J.; Kim, D. J.; Yang, S. M.; Yoon, D.; Cheong, H.; Chang, K.-S.; Noh, T. W.; Bu, S. D. Ferroelectricity in highly ordered arrays of ultra-thin-walled $Pb(ZrTi)O_3$ nanotubes composed of nanometer-sized perovskite crystallites. *Nano Lett.* **2008**, *8*, 1813−1818.
(29) Suchanicz, J.; Ptak, W. S. On the phase transition in $Na_{0.5}$ $Bi_{0.5}$ TiO_3. *Ferroelectr., Lett.* **1990**, *12*, 71−78.
(30) Hamieh, A.; Ponchel, F.; Barrau, S.; Remiens, D. Synthesis of lead-free $(Bi_{0.5}Na_{0.5})$ TiO_3 thin film by RF magnetron sputtering: Impact of Na on the properties of film. *Ferroelectrics* **2020**, *556*, 79−86.
(31) Ghasemian, M. B.; Lin, Q.; Adabifiroozjaei, E.; Wang, F.; Chu, D.; Wang, D. Morphology control and large piezoresponse of hydrothermally synthesized lead-free piezoelectric $(Bi_{0.5}Na_{0.5})TiO_3$ nanofibers. *RSC Adv.* **2017**, *7*, 15020−15026.
(32) Suzer, S.; Ertas, N.; Ataman, O. Y. XPS characterization of Bi and Mn collected onatom-trapping silica for AAS. *Appl. Spectrosc.* **1999**, *53*, 479−482.
(33) Zhang, G.; Yang, J.; Zhang, S.; Xiong, Q.; Huang, B.; Wang, J.; Gong, W. Preparation of nanosized Bi_3NbO_7 and its visible-light photocatalytic property. *J. Hazard. Mater.* **2009**, *172*, 986−992.
(34) Inceesungvorn, B.; Teeranunpong, T.; Nunkaew, J.; Suntalelat, S.; Tantraviwat, D. Novel $NiTiO_3/Ag_3VO_4$ composite with enhanced photocatalytic performance under visible light. *Catal. Commun.* **2014**, *54*, 35−38.
(35) Xu, X.; Xie, Y.; Ni, S.; Azad, A. K.; Cao, T. Photocatalytic H2 production from spinels $ZnGa_{2-x}Cr_xO_4$ ($0 \le x \le 2$) solid solutions. *J. Solid State Chem.* **2015**, *230*, 95−101.

(36) Chen, Z.; Yuan, C.; Liu, X.; Meng, L.; Cheng, S.; Xu, J.; Zhou, C.; Wang, J.; Rao, G. Optical and electrical properties of ferroelectric $Bi_{0.5}Na_{0.5}TiO_3$-$NiTiO_3$ semiconductor ceramics. *Mater. Sci. Semicond. Process.* **2020**, *115*, 105089.
(37) Han, H.; Park, S.-J.; Jang, J. S.; Ryu, H.; Kim, K. J.; Baik, S.; Lee, W. In situ determination of the pore opening point during wet-chemical etching of the barrier layer of porous anodic aluminum oxide: nonuniform impurity distribution in anodic oxide. *ACS Appl. Mater. Interfaces* **2013**, *5*, 3441−3448.
(38) Lee, W.; Park, S.-J. Porous anodic aluminum oxide: anodization and templated synthesis of functional nanostructures. *Chem. Rev.* **2014**, *114*, 7487−7556.
(39) Wang, Z. L.; Song, J. Piezoelectric nanogenerators based on zinc oxide nanowire arrays. *Science* **2006**, *312*, 242−246.
(40) Bernal, A.; Bassiri-Gharb, N. Piezoresponse force microscopy characterization of high aspect ratio ferroelectric nanostructures. *J. Appl. Phys.* **2012**, *112*, 052012.
(41) Wu, S.; Zhang, J.; Liu, X.; Lv, S.; Gao, R.; Cai, W.; Wang, F.; Fu, C. Micro-area ferroelectric, piezoelectric and conductive properties of single $BiFeO_3$ nanowire by scanning probe microscopy. *Nanomaterials* **2019**, *9*, 190.
(42) Zhu, Z.; Li, J.; Li, S.; Li, C. Investigation of the mechanism of domain switching in different $Na_{0.5}Bi_{0.5}TiO_3$ microstructures. *Ceram. Int.* **2019**, *45*, 17495−17501.
(43) Song, J. M.; Luo, L. H.; Dai, X. H.; Song, A. Y.; Zhou, Y.; Li, Z. N.; Liang, J. T.; Liu, B. T. Switching properties of epitaxial La0.5Sr0.5CoO3/Na0.5Bi0.5TiO3/La0.5Sr0.5CoO3 ferroelectric capacitor. *RSC Adv.* **2018**, *8*, 4372−4376.
(44) Wang, F.; Wang, J. B.; Zhong, X. L.; Li, B.; Zhou, Y. C. Synthesis and characterization of Bi3.15Nd0.85Ti3O12 nanotube arrays. *J. Cryst. Growth* **2009**, *311*, 4495−4498.
(45) Liu, X.; Li, M.; Hu, Z.; Zhu, Y.; Dong, S.; Zhao, X. Preparation and properties of the CoFe2O4/Bi3.15Nd0.85Ti3O12 multiferroic composite coaxial nanotubes. *Mater. Lett.* **2012**, *82*, 57−60.
(46) Cai, W.; Lu, X.; Bo, H.; Kan, Y.; Weng, Y.; Zhang, L.; Wu, X.; Huang, F.; Eng, L. M.; Zhu, J.; Yan, F. Ferroelectric and dielectric properties of Bi3.15Nd0.85Ti3O12 nanotubes. *J. Appl. Phys.* **2011**, *110*, 052004.
(47) Scott, J. F.; Dawber, M. Oxygen-vacancy ordering as a fatigue mechanism in perovskite ferroelectrics. *Appl. Phys. Lett.* **2000**, *76*, 3801−3803.
(48) Grossmann, M.; Lohse, O.; Bolten, D.; Boettger, U.; Schneller, T.; Waser, R. The interface screening model as origin of imprint in PbZrxTi1-xO3 thin films. I. Dopant, illumination, and bias dependence. *J. Appl. Phys.* **2002**, *92*, 2680−2687.
(49) Kim, Y.; Kumar, A.; Ovchinnikov, O.; Jesse, S.; Han, H.; Pantel, D.; Vrejoiu, I.; Lee, W.; Hesse, D.; Alexe, M.; Kalinin, S. V. First-order reversal curve probing of spatially resolved polarization switching dynamics in ferroelectric nanocapacitors. *ACS Nano* **2011**, *6*, 491−500.

NOTE ADDED AFTER ASAP PUBLICATION

This paper was published on January 24, 2021, with an error in a scale bar in Figure 6(a). The corrected version was reposted on January 27, 2021.

https://dx.doi.org/10.1021/acsanm.0c02878
ACS Appl. Nano Mater. 2021, 4, 1294−1304